

Final Draft
of the original manuscript:

Gombola, C.; Hasemann, G.; Kauffmann, A.; Sprenger, I.; Laube, S.; Schmitt, A.; Gang, F.; Bolbut, V.; Oehring, M.; Blankenburg, M.; Schell, N.; Staron, P.; Pyczak, F.; Krüger, M.; Heilmaier, M.:

A zone melting device for the in situ observation of directional solidification using high-energy synchrotron x rays editors-pick.

In: Review of Scientific Instruments. Vol. 91 (2020) 9, 093901

First published online by AIP: 01.09.2020

<https://dx.doi.org/10.1063/5.0019020>

A zone melting device for the in-situ observation of directional solidification using high-energy synchrotron X-rays

C. Gombola¹, G. Hasemann², A. Kauffmann¹, I. Sprenger¹, S. Laube¹, A. Schmitt¹, F. Gang¹, V. Bolbut², M. Oehring³, M. Blankenburg³, N. Schell³, P. Staron³, F. Pyczak³, M. Krüger², M. Heilmaier¹

¹ Karlsruhe Institute of Technology (KIT), Institute for Applied Materials (IAM-WK), Engelbert-Arnold-Str. 4, 76131 Karlsruhe, Germany

² Otto von Guericke University, Institute for Materials & Joining Technology, Universitätsplatz 2, 39106 Magdeburg, Germany

³ Helmholtz-Zentrum Geesthacht, Institute of Materials Research, Max-Planck-Str. 1, 21502 Geesthacht, Germany

Abstract

1 Directional solidification (DS) is an established manufacturing process to produce high-
2 performance components from metallic materials with optimized properties. Materials for
3 demanding high-temperature applications, for instance in energy generation and aircraft engine
4 technology, can only be successfully produced using methods such as directional solidification.
5 It has been applied on an industrial scale for a considerable amount of time, but advancing this
6 method beyond the current applications is still challenging and almost exclusively limited to
7 post-process characterization of the developed microstructures. For a knowledge-based
8 advancement and a contribution to material innovation, in-situ studies of the DS process are
9 crucial using realistic sample sizes to ensure scalability of the results to industrial sizes.
10 Therefore, a specially designed Flexible Directional Solidification (FlexiDS) device was
11 developed for use at the P07 High Energy Materials Science (HEMS) beamline at PETRA III
12 (Deutsches Elektronen-Synchrotron (DESY); Hamburg, Germany). In general, the process
13 conditions of the crucible-free, inductively heated FlexiDS device can be varied from 6 to
14 12000 mm/h (vertical withdrawal rate) and from 0 to 35 rpm (axial sample rotation). Moreover,
15 different atmosphere like Ar, N₂, vacuum can be chosen for the process. The maximum
16 temperature the device was designed for is 2200 °C. This unique device allows in-situ
17 examination of the directional solidification process and subsequent solid-state reactions by X-
18 ray diffraction in the transmission mode. Within this project, different structural intermetallic
19 alloys with liquidus temperatures up to 2000 °C were studied in terms of liquid-solid regions,
20 transformations and decompositions, with varying process conditions.

21

1 Introduction

22 Directional solidification has been applied on an industrial scale, mostly to Nickel-based
23 superalloys, since the 1970s [1]. Especially for high temperature materials, used under creep
24 conditions, directional solidification is a promising process. During processing, the established
25 liquid zone of the sample moves out of the hottest zone and is subjected to temperature gradient.
26 Due to that single-crystalline components or components at least exhibiting an elongated
27 microstructure parallel to the loading direction form. Transversely oriented grain boundaries as
28 source of creep pores and, therefore, creep rupture can be reduced or even eliminated [1]. For
29 example, incorporating an aligned second phase (e.g. Cr or Mo) into NiAl [2,3] improves the
30 creep resistance along the growth direction and increases the damage tolerance by toughening.
31 These alloys were often produced by a Bridgman-typ directional solidification apparatus, where
32 the heated crucible rest on a water-cooled copper base. Lowering the base with a specific rate
33 provide a movement of the melt from the hot zone into a liquid metal bath [4-7]. Another
34 technique used is an optical floating zone furnace. Here the heating source is a xenon arc-lamp
35 emitting infrared radiation which is focused on the specimen enclosed in a quartz tube [2,3,8].
36 Ref. [9,10] produced directionally solidified specimens in a crucible-free mode by
37 electromagnetically levitated zone process. A crucible-free process offers the advantage of no
38 contamination/reaction from the crucible with the sample even at very high temperatures.
39 Even though directional solidification has been applied on an industrial scale, advancing this
40 method beyond the current applications is still challenging. Moreover, the conventional casting
41 and directional solidification processes are not suitable for all high-temperature materials
42 beyond Nickel-based superalloys. A limiting factor is a possible reaction of the material with
43 the crucible at such elevated temperatures. Novel materials or changes in the components
44 require significant changes in the process parameters, which is mostly done on a trial-and-error
45 basis. A knowledge-based advancement of the process is difficult, as – at least to some extent
46 – there is no possibility to characterize the production process as well as the materials behavior
47 “in-situ”. Investigations are almost exclusively limited to a post-process characterization of the
48 microstructures, which are often not the same as directly formed by cooling short below the
49 solidus line.

50 X-ray diffraction methods are suitable for in-situ studies of the DS process. With these
51 techniques, the investigation of the liquid zone and solidification front is possible in
52 transmission mode. Due to the high temperatures and the difficulties in handling sufficient
53 amounts of hot melt, studies of the melting and solidification behavior so far have almost
54 exclusively been performed for metals or alloys with rather low melting points, e.g. magnesium

55 or gallium-indium alloys [11-13]. Our crucible-free, inductively heated FlexiDS device allows
56 in-situ studies of the synthesis, transformation, and decomposition of various structural
57 intermetallic materials with maximum liquidus temperatures of 2200 °C via diffraction of high-
58 energy synchrotron radiation. The maximum sample diameter is 14 mm, which is a compromise
59 between possible X-ray transmission and a process that is close enough to relevant industrial
60 processes concerning temperature distribution in the solid and convection in the melt. The
61 device has been designed for the use at the P07 High Energy Materials Science (HEMS)
62 beamline at PETRA III (Deutsches Elektronen-Synchrotron (DESY); Hamburg, Germany),
63 where the combination of a high photon flux ($>10^{12}$ 1/s) and fast readout 2D detectors (15 Hz)
64 enables the study of this complex liquid-solid interactions during solidification and subsequent
65 solid-state reactions. The available detectors cover a range up to 250 Hz, corresponding to a
66 temporal resolution of 4 ms. However, 250 Hz is never needed with thick samples. The high
67 beam energy of typically 100 keV allows transmission of samples with various diameters (14
68 to 8 mm) and densities typically between TiAl and Mo-based alloys. A large portion of
69 reciprocal space can be investigated at rapid acquisition times (typically 1-30 s, depending on
70 the sample size and alloy system). This technical environment enables to investigate the local
71 evolution of the microstructure during directional growth depending on different process
72 conditions (withdrawal rate and rotation speed, rod diameter).
73 In the following, the directional solidification device and its use for characterizing the processes
74 occurring during solidification is described in detail. This provides the base for an
75 understanding of solidification and the development of alloys, which are produced by
76 directional solidification.

2 Technical layout of the FlexiDS device

77 The DS device is in essence independent and can, thus, be used either in the laboratory or it can
78 be integrated at a beamline (here: P07 High Energy Materials Science (HEMS) beamline at
79 PETRA III). In order to perform in-situ investigations during directional solidification with the
80 required flexibility, the device has to fulfill both, the requirements of the directional
81 solidification process as well as the additional demands for combining this process technology
82 with X-ray diffraction geometries.

83 A schematic drawing of the main modules of the device is visualized in Figure 1. The
84 mechanical set-up manufactured by SYSTEC Fertigungstechnik GmbH & Co. KG [14]
85 includes the following modules: I) directional solidification device on a positioning stage, II)
86 energy supply and vacuum pump, III) water battery (Figure 1). All components are designed

87 for flexible set-up and transport. Therefore, a precise positioning of the chamber with respect
88 to the X-ray beam is possible. For the directional solidification process, a clean and protective
89 atmosphere is essential to protect the material from oxidation and contamination. For the sake
90 of clarity, Figure 2 gives an overview of the complex device with all components and features.
91 Important features and parameters are compiled in the following list:

- Atmosphere: Ar, N₂, vacuum
- Heating: inductive
- Power: 12 kW (150...375 kHz)
- T_{max}: 2200 °C (tested 2000 °C)
- Rod-shaped samples from 8 to 14 mm in diameter

Available solidification parameter:

- Vertical withdrawal rate: 6 - 12000 mm/h (6 mm/h increment, tested so far 6 - 360 mm/h)
- Axial sample rotation 0 - 35 rpm (1 rpm steps), synchronous rotation or counter rotation

Temperature observation:

- two pyrometers positioned at the liquid zone (in the coil) and 10 mm above

The manually controlled power of 12 kW is spread from 0 to 100 % and can be adjusted in 0.1 % steps, which enables the user to reach and maintain the sample in a liquid state.

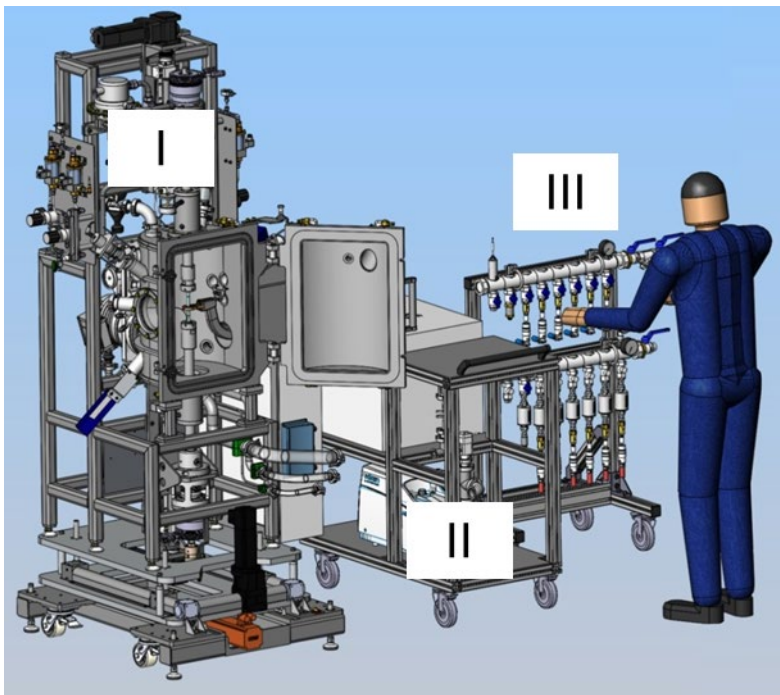


Figure 1: Schematic of the modules of the setup: I) Directional solidification device on positioning stage, II) Energy supply and vacuum pump, III) Water battery. The person is displayed here to estimate the size and usability of the device.

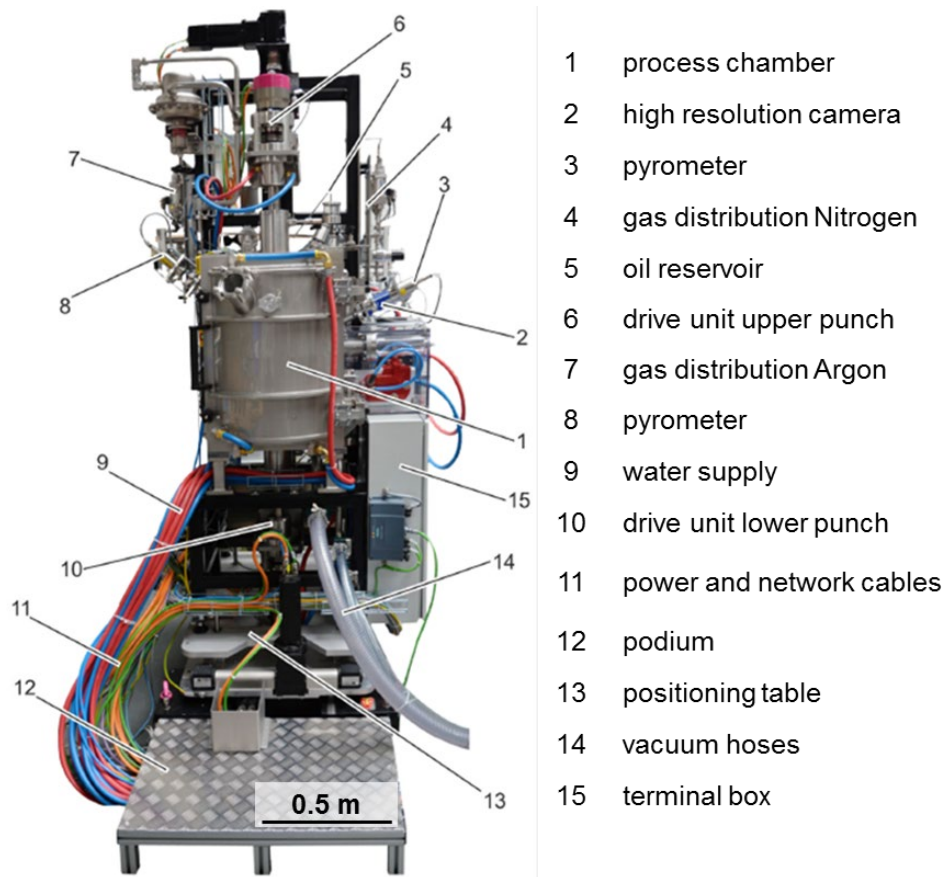


Figure 2: Overview of the zone melting device with its components.

2.1 Process chamber

A visual inspection of the process chamber interior is possible via multiple windows and a lamp illuminating the chamber. Furthermore, the process chamber can be monitored via two high-resolution cameras suitable for high temperature image acquisition (detailed description in section 3). These cameras may also be used to observe the liquid zone of the sample. Two pyrometers detect the temperature of the rod inside the coil and at an adjustable distance above the coil (typically 10 mm above the induction coil). With this arrangement, the temperature can be measured in the liquid zone and in 10 mm distance, usually already in the solid state of the sample. With the assumption of linear temperature decrease, a temperature gradient can be determined. The temperature evolution plays an important role in terms of process control and power adjustment. Spare flanges can be used for additional measuring devices or other attachments. One is located at the chamber door (DN 25 ISO-KF) (Figure 2) and a second at the backside of the chamber (DN 40 ISO-KF) (Figure 3). Figure 3 shows the interior view of the chamber. For the sake of safety and sealing, the process chamber door is equipped with two locks. Moreover, a door protection switch is attached which prevents that process gas flow and heating is activated if the process chamber door is open.

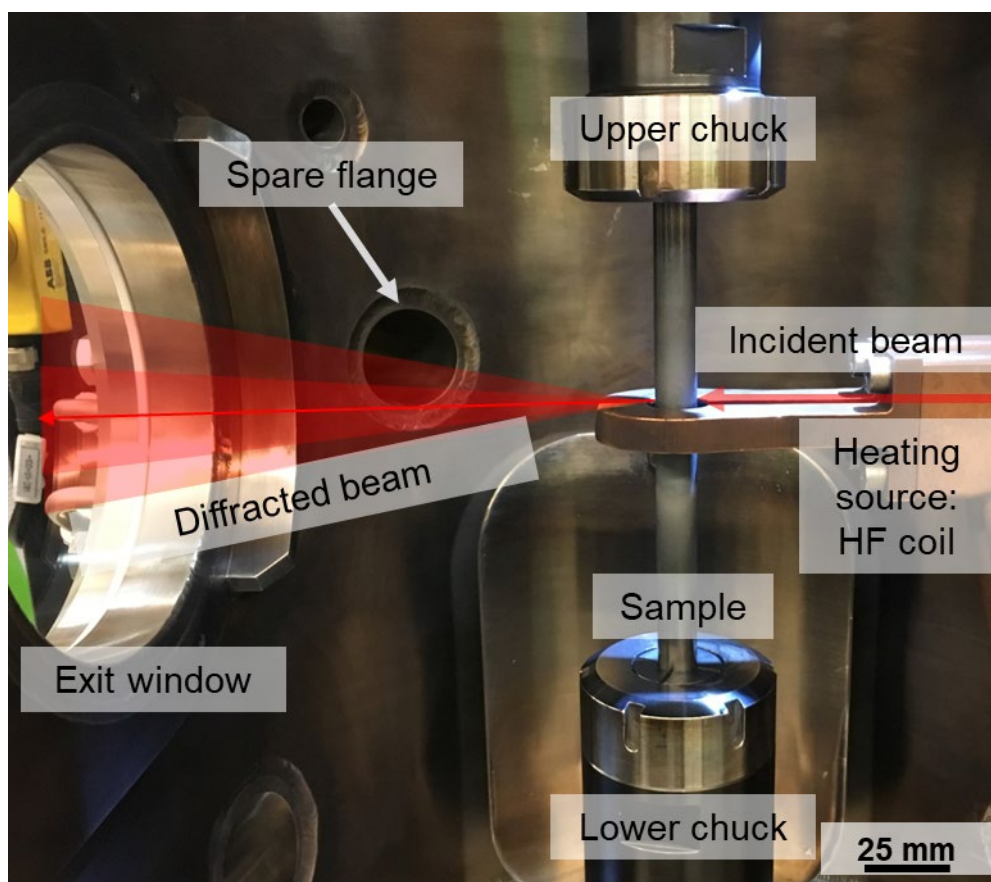


Figure 3: Interior of the process chamber: The water-cooled chucks and the high frequency (HF) coil as the heating source are highlighted. The X-ray beam enters the chamber on the right side, interacts with the sample and the diffracted beam leaves the chamber on the left side through the larger window.

109

2.2 Sample holder and induction coil

110 The sample passes through the induction coil (Figure 3) and is fixed in the upper and lower
 111 drive shaft by clamping jaws. 10 mm of the sample are needed on both ends for mounting the
 112 sample in the clamping system. Together with a typical safety distance of 20 mm from the coil
 113 below and above preventing induction in the clamps, the sample length is calculated. The upper
 114 chuck is tightened manually while the lower one has a pneumatic system in order to allow the
 115 sample to expand during heating up and to tighten it right before the liquid zone forms. With
 116 the two independent drive shafts, a vertical movement of the sample and synchronous or counter
 117 rotation can be applied. The induction coil displayed schematically in Figure 4a was specially
 118 designed for in-situ experiments and is suitable for the above-mentioned sample geometries.
 119 An integrated water circuit achieves cooling of the coil, chucks and housing. The conical recess
 120 in the coil prevents cutting off for the diffracted beam to pass (Figure 4a). Figure 4b gives an
 121 insight into the chamber during heating. For the in-situ experiments, the samples were usually
 122 moved upward (lifted) through the coil due to the position of the beam and the recess of the

123 coil. Thus, the upper sample part represents the directionally solidified part and the lower part
124 is called the feed, which is in the as-cast condition. For the results shown in section 5, both parts
125 of the rod are rotated with the same speed and direction, but these two parameters can be also
126 varied independently.

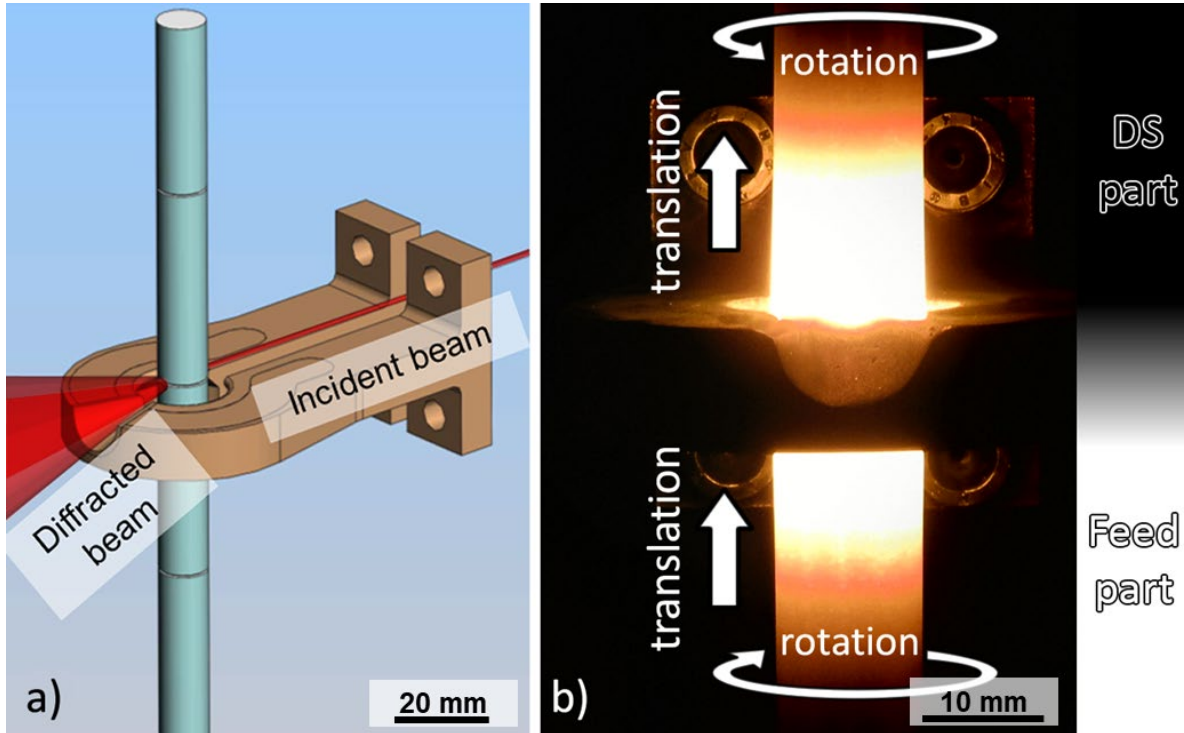
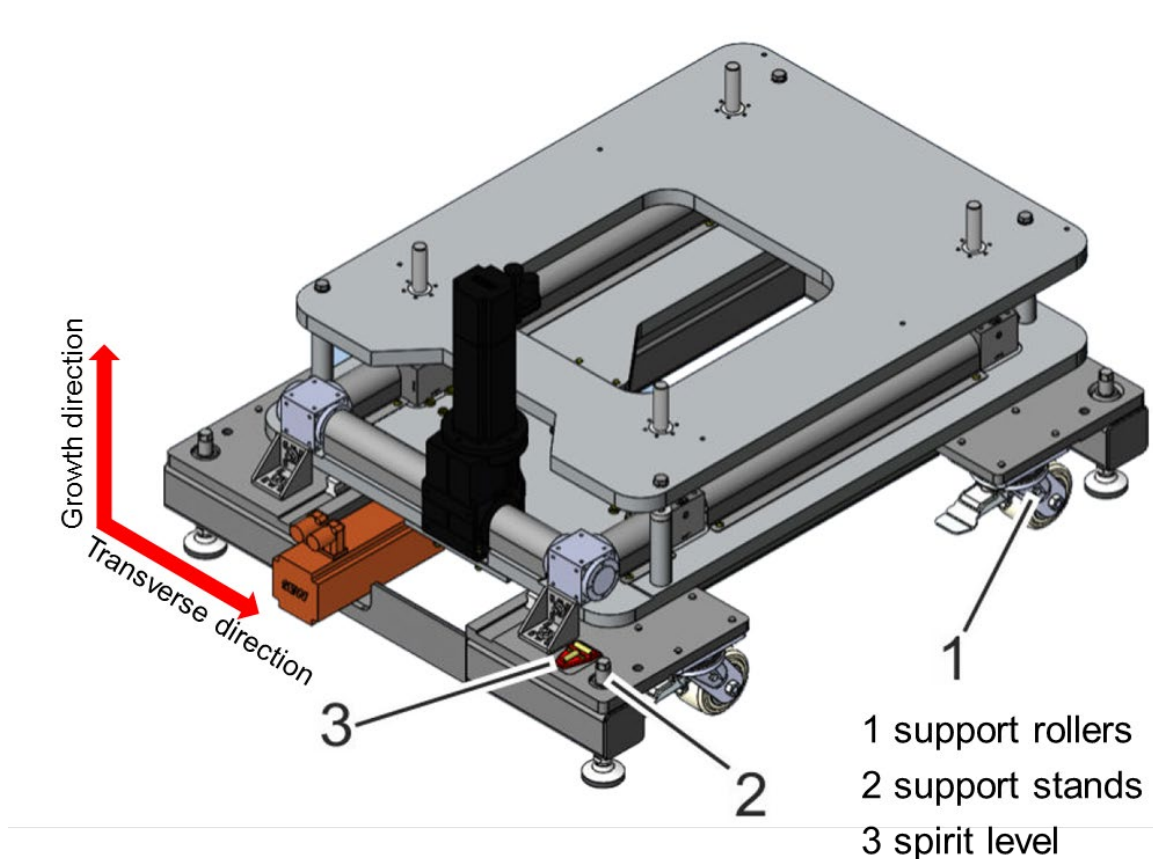


Figure 4: a) Detail of the specifically designed HF coil, b) HF coil and a heated sample during processing. Arrows indicate the process movement in terms of withdrawal rate and rotation speed.

127

2.3 Positioning stage

128 In order to move the FlexiDS process chamber with respect to the incident beam parallel as
129 well as transverse to the samples' growth direction, the system is mounted on a positioning
130 stage (Figure 5). Once placed with support rollers at the final position, the device is set on the
131 support stands, which are located at the corners of the stage. A spirit level facilitates the
132 adjustment and ensures the horizontal alignment. The movement range is ± 50 mm in growth
133 direction and transverse to growth direction. The smallest positioning increment is 0.05 mm
134 allowing an accurate positioning with respect to the incoming beam.



135

Figure 5: Positioning stage, range of motion is ± 50 mm parallel and transverse to growth direction.

136

3 Workstations and control software

137 Two workstations, a mobile panel and a PC workstation, are connected to the device. The
 138 control software is implemented by iTG Induction systems [15]. Generally, two modes of
 139 operation are possible: “manual mode”, mainly operating the mobile panel, and “auto mode”,
 140 mainly suited for the PC control during in-situ experiments.

141 The mobile panel next to the chamber allows fast and precise setting up and positioning of the
 142 sample. In order to achieve the correct position of the sample with respect to the induction coil,
 143 the upper and the lower driving shaft are controlled individually. Apart from the actuators, the
 144 coil power, the vacuum pumps and the gas flow can be controlled from the mobile panel in
 145 “manual mode”.

146 The spatial separation of device and PC process control is necessary for the in-situ observations
 147 during directional solidification. By activating the “auto mode” the vacuum pumps
 148 automatically turns on and the chamber is evacuated to $2 \cdot 10^{-5}$ mbar, once the sample is
 149 placed in the device and the door is properly closed. In a second step, the process chamber is
 150 purged with Ar. During the DS process, Ar flow is active. The PC workstation controlling the

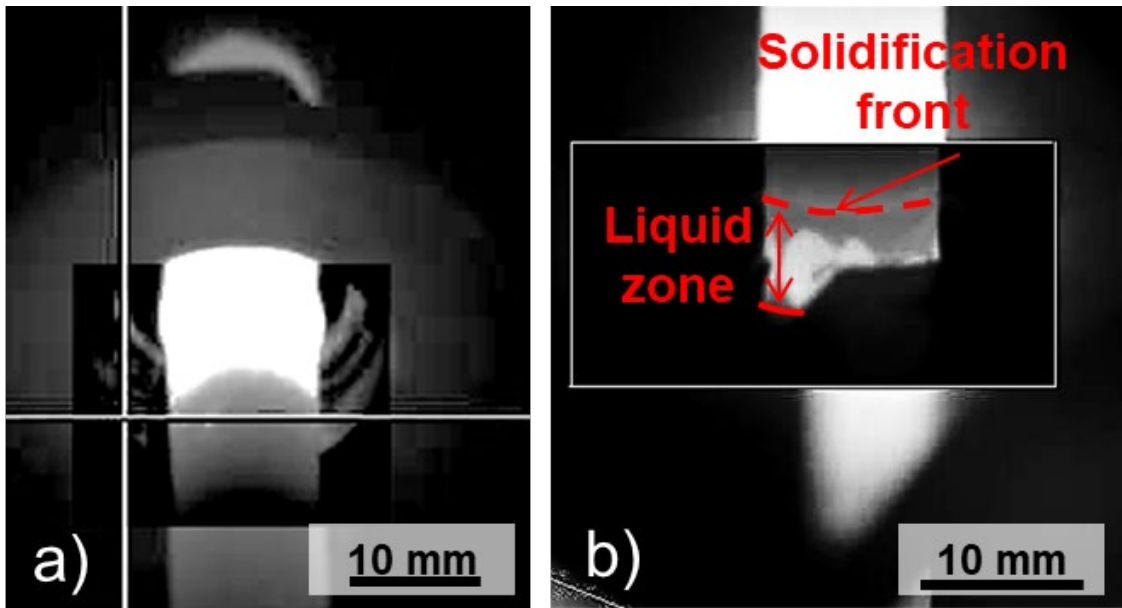
151 device consists of process parameter control like withdrawal rate, rotation speed, coil power as
152 well as movement of the positioning stage. A detailed camera view of the sample (Figure 6)
153 and pyrometers are incorporated in the PC controlling unit. Within the “auto mode”, the process
154 control software saves all parameters and the corresponding changes with timestamps in a log
155 file.

156 For in-situ observations during the process, a second person is recommended to adjust the beam
157 and to run the recording of the diffraction data.

158 The reaction of the sample to power adjustments can be observed with the high dynamic range
159 cameras (hema electronic GmbH, Germany, type **seelector**ICAM weld [16]). One is placed to
160 give information from below the coil and the second one to show a view from above the coil.

161 The cameras are sensitive to temperatures below 1000 °C and the contrast can be adjusted for
162 an optimal visual representation. The lenses C2514-M (KP)/Ricoh FL-CC2514-2M - 1.4/25mm
163 from Pentax ensure a balance between clarity and details of the liquid zone. The pyrometers
164 utilized for our device measure temperatures between 1000 and 3000 °C (LumaSense
165 Technologies GmbH, Germany, type IMPAC pyrometers ISQ 5 [17]). In the “LumaSense”
166 software data of both pyrometers is plotted in a temperature vs. time diagram. Temperature
167 measurement is necessary to control the process and gives information about the temperature
168 gradient within the sample. Examples of the detailed camera view during the process are given
169 in Figure 6a and b, from below and from above the coil, respectively. Both information are
170 crucial for process control. In order to establish a stable liquid zone sufficient power and
171 overheating is required. When the power level is too high, depending on the liquid surface
172 tension, locally an expansion of the liquid zone arises (Figure 6a). The surface features in
173 Figure 6b are oxide scales forming due to the oxygen in the sample. It appears brighter than the
174 liquid beneath. Thus, these oxides visualize the movement and the overheating of the liquid
175 zone and may serve as indicators during the process.

176



177

Figure 6: Visualization of the sample from two different points of view: (a) below the coil and (b) above the coil. The insert is a so-called region of interest (ROI). The settings only for this region is can be adjusted variable separately from the general settings of the image.

178

4 System integration at the P07 High Energy Materials Science Beamline

179 The modules are placed in the experimental hutch 3 (EH3) at the beamline P07 at DESY in
 180 Hamburg as illustrated in Figure 7a. The X-ray beam transmits the chamber from the right to
 181 the left in Figure 7a and b. After the interaction with the sample, the diffracted beam leaves the
 182 chamber through the larger window on the left side of the chamber and is captured by the
 183 detector placed in a certain distance from the sample. It is noteworthy that because of the
 184 crucible-free set-up and the recess in the coil the incident beam is only diffracted by the sample
 185 (without any alien reflections). This facilitates the evaluation of the diffraction data. Diffraction
 186 resulting from the windows are negligible. The on-site infrastructure, which allows beam and
 187 detector control, is used for the X-ray diffraction data acquisition.

188 The X-ray energy at P07 is tunable from 30 keV to 200 keV with its main optics consisting of
 189 a water-cooled double crystal monochromator in horizontal Laue scattering geometry. The
 190 energy resolution ($\Delta E/E$) ranges from 1×10^{-3} down to 7×10^{-5} by changing the curvature of
 191 the bent Si (111) crystals in Rowland geometry and/or inserting a channel-cut crystal. The spot
 192 size can be varied from $1 \text{ mm} \times 1 \text{ mm}$ (unfocused beam) down to $2 \mu\text{m}$ vertical \times $30 \mu\text{m}$
 193 horizontal (focused beam via Al Compound Refractive Lenses) in high-beta mode or up to
 194 0.9 mm vertical \times 6 mm horizontal in low-beta mode, where the beta mode is switched by

195 changing the beta function at the undulator source position. The maximum flux currently
196 reaches 7×10^{11} ph/s at 100 keV [18,19].

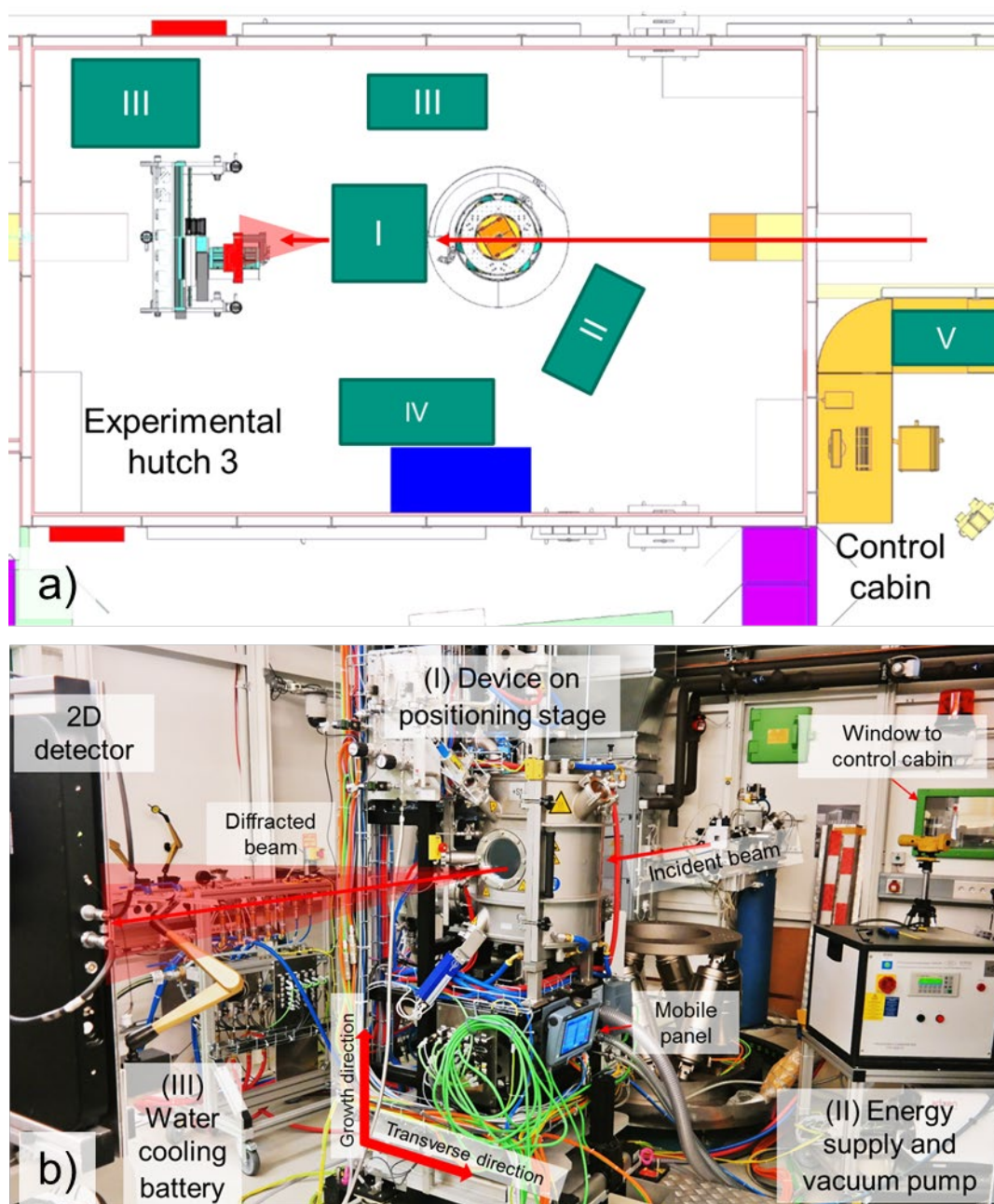
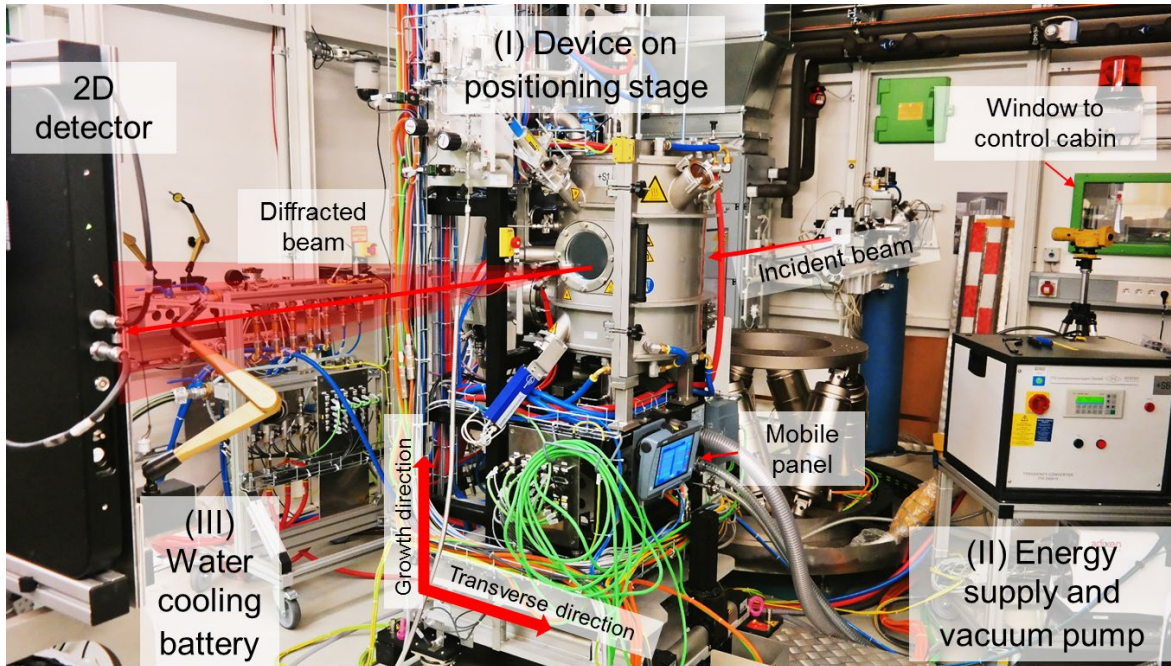


Figure 7: a) Ground plan of the experimental hutch 3 with the installed modules of the zone melting set-up: (I) device on positioning stage, (II) energy supply and vacuum pump, (III) water cooling battery and chiller, (IV) the control board, (V) PC workstation. b) Illustration of the experimental setup at the P07 beamline at PETRA III, DESY Hamburg.

197



198

4.1 X-ray diffraction performance

199 Within the project, five material systems, as indicated in the first column of Table 1 and several
 200 alloy compositions of each system were investigated. The different content of heavy elements
 201 in the systems provoke significantly different transmission behavior. Thus, exposure times have
 202 to be adapted to the respective material (Table 1). The signal to noise ratio obtained by
 203 maximum intensity and background for all investigated alloy systems is given in the last column
 204 of Table 1. A beam size of $1 \text{ mm} \times 0.5 \text{ mm}$ was used to achieve sufficient grain statistics and
 205 conveniently short exposure times. A Perkin Elmer XRD 1621 solid-state detector with
 206 2048×2048 pixels and a pixel size of $200 \mu\text{m} \times 200 \mu\text{m}$ was used for all measurements. As
 207 seen in Table 1 a photon energy between 98 and 103.6 keV was used, corresponding to
 208 wavelengths between 0.126 and 0.119 Å. The detector was located in approximately 1.9 m
 209 distance from the sample. The resulting maximum 2θ angle was 6° and the step size is 0.006° .
 210 Si and CeO_2 powder, were used as reference to calibrate the measurements.

211

Table 1: Experimental parameters for the investigated materials.

Material	Photon energy [keV]	Beam size [b mm × h mm]	Exposure time [s]	Signal to noise ratio [a.u.]
Fe-Al [20]	98	1 x 0.5	2 – 3	60 – 120
Nb-Si-Cr [21]	98	1 x 0.5	20 – 30	28 – 34
NiAl-Cr,Mo[22]	98 – 103.6	1 x 0.5	1 – 12	75 – 225

Mo-Si-B [23]	98 – 103.6	1 x 0.5	6 – 32	22 – 172
TiAl [24]	98 – 103.6	1 x 0.5	2 – 6	105 – 135

5. Examples of in-situ X-ray diffraction experiments during directional solidification

212 In the following, two examples for in-situ investigation of directional solidification of high
 213 melting point two-phase intermetallic materials are given. The first case focuses on the Ti-Al
 214 system, or more precisely on so-called γ -TiAl-alloys which have been commercialized already
 215 in investment cast, isothermally forged as well as in additively manufactured (by EBM) form
 216 [25-28]. DS might enable a unique combination of high creep strength and ductility [28], but
 217 the decisive processing parameters are still unknown. The second case considers a high Al-
 218 containing two-phase FeAl alloy, which undergoes a high temperature eutectoid decomposition
 219 reaction upon solidification via a peritectic reaction. Here, the overarching scientific question
 220 is whether the eutectoid lamellae can be properly aligned during DS in order to also create
 221 creep-resistant microstructures at elevated temperatures. All chemical compositions mentioned
 222 in what follows are given in at.%.

5.1 The Ti-Al system

223 As mentioned above DS is an attractive processing method for γ -TiAl-alloys because it allows
 224 to align the constituting phases of the material [29]. However, the knowledge about suitable
 225 processing conditions is limited. For example, the effects of different alloy compositions on the
 226 solidification process are still not well understood. In-situ investigations are a powerful tool to
 227 get a deep insight into the solidification of TiAl alloys. All the more as it is difficult to yield
 228 information on the solidification process from investigations at room temperature because
 229 subsequent solid-state phase transformations will mask the high-temperature situation to a
 230 significant extent.

231 An example of investigations on TiAl alloys is an experimental proof of the predictions for
 232 solidification [24], which were made based on the „nucleation and constitutional
 233 undercooling“-model of Hunziker et al. [30]. If correct, a strong dependence of the type of the
 234 solidifying phase as well as its morphology on the G/v ratio should be found (G: temperature
 235 gradient, v: withdrawal rate). Solidification experiments with varying withdrawal rate between
 236 some mm/h up to some hundreds mm/h were performed with different binary TiAl-alloys. Ti-
 237 45Al solidifies via the β -phase (see phase diagram Figure 8). For this alloy a change from planar
 238 to dendritic solidification with increasing withdrawal rate (decreasing G/v ratio) is predicted
 239 (Figure 9a). The other alloy, Ti-48Al, also changes from planar to dendritic solidification mode

240 with increasing withdrawal rate, but the solidifying phase is additionally predicted to change
 241 from α -phase to a two-phase α/β mixture. From the diffraction ring patterns as shown in
 242 Figure 9b and c, it is obvious that for Ti-48Al the change of the solidifying phase from α -phase
 243 to a two-phase α/β mixture with increasing withdrawal rate is experimentally verified. For a
 244 withdrawal rate of 36 mm/h only reflections of melt (L) and α -phase were present. α - and β -
 245 phase solidify simultaneously from the melt for an increased withdrawal rate of 360 mm/h,
 246 however the change in phase constitution occurs at a significantly lower G/v value as obtained
 247 by the model. The numerical difference might originate from improper model parameters, but
 248 this question is beyond the scope of the present work. Also other predicted effects such as a
 249 change of the solidification morphology from planar to dendritic with increasing withdrawal
 250 rate were confirmed in Ti-48Al as well as in Ti-45Al, although in the former case it occurred
 251 again at a lower G/v value than obtained by the model (Figure 9a). In summary, by in-situ
 252 studies it can easily be analysed at which conditions certain phases and morphologies will form
 253 in TiAl alloys during solidification without being constrained by indirect conclusions as it is
 254 the case in post process investigations.

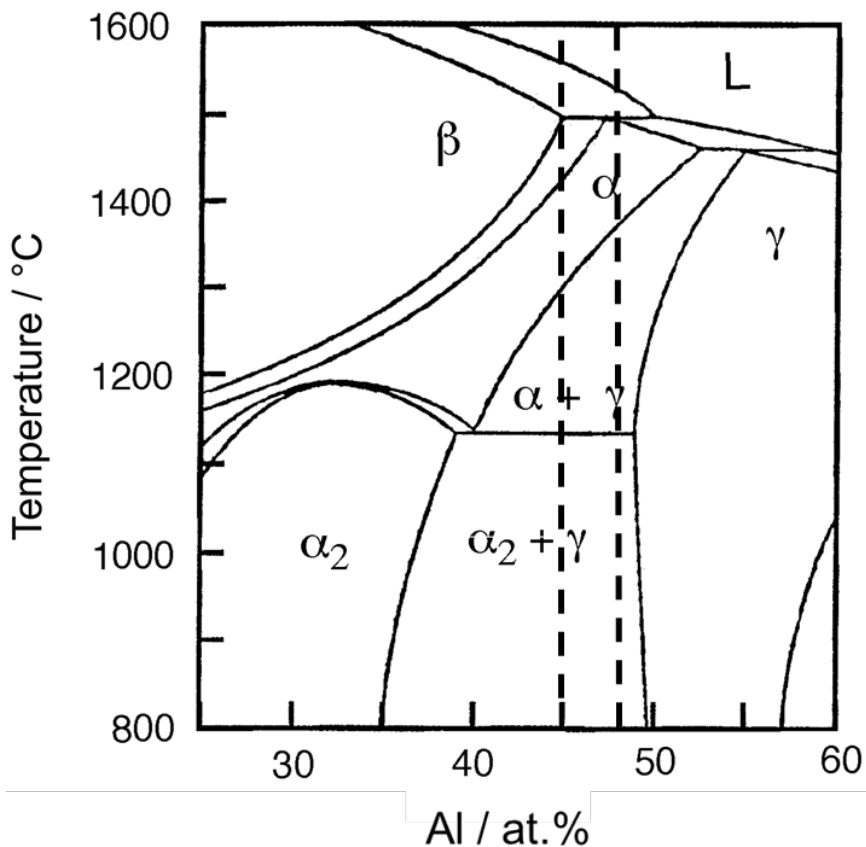


Figure 8: Section of the equilibrium Ti-Al phase diagram [31].

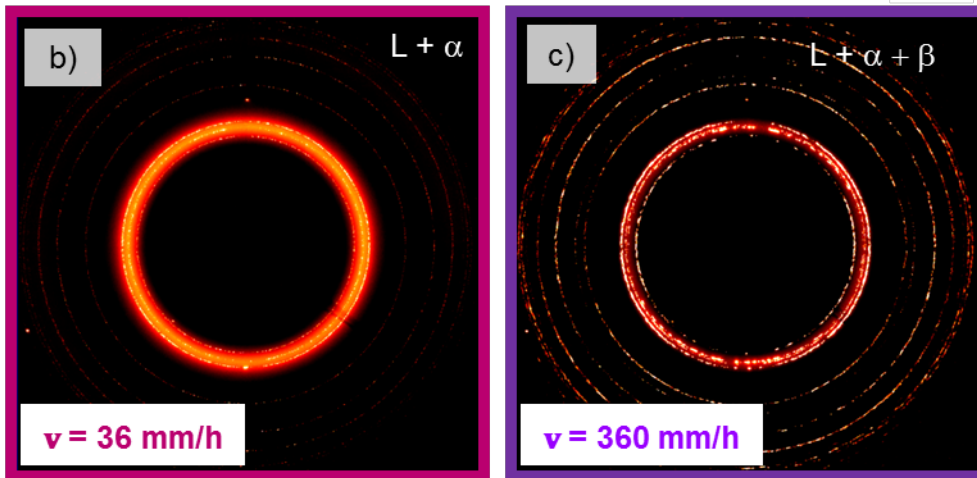
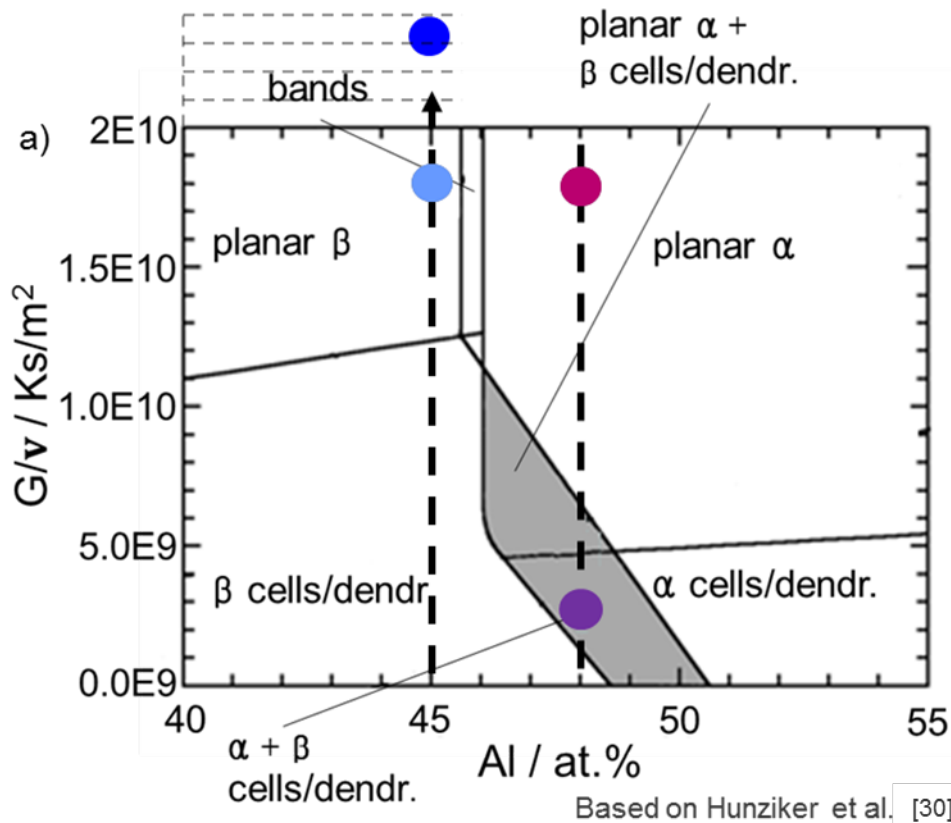


Figure 9: a) Predicted solidification morphology and solidifying phases in dependence on G/v and alloy composition. Resulting G/v values in the experiments are indicated by dots. Diffraction pattern of the solidification front of Ti-48Al at different withdrawal rates, b) 36 mm/h and c) 360 mm/h.

255

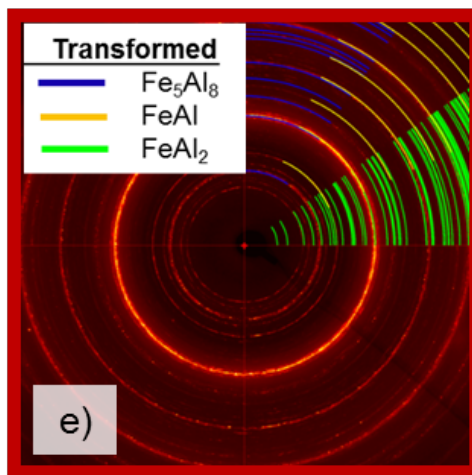
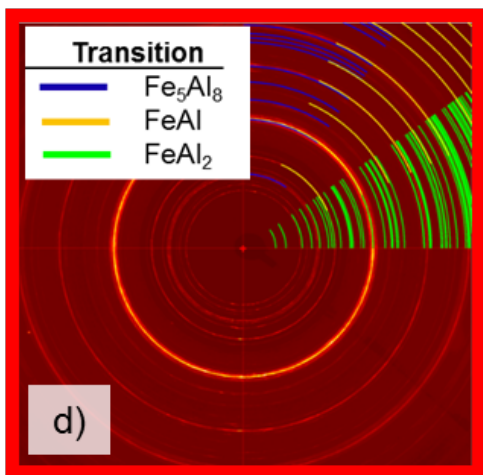
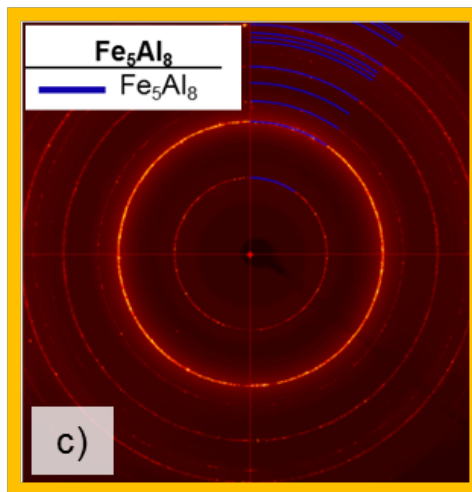
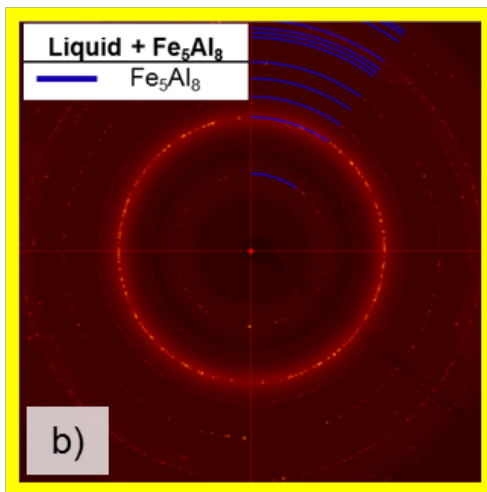
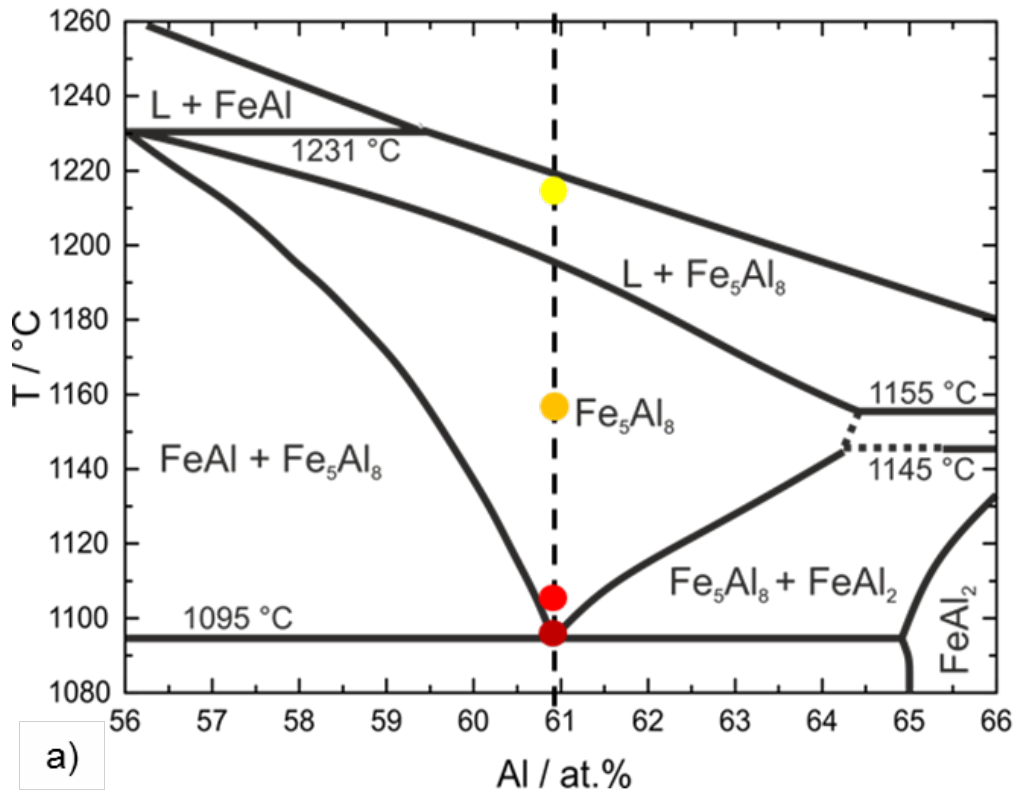
5.2 The Fe-Al system

256 In Fe-61Al, an eutectoid decomposition Fe_5Al_8 (Cu_5Zn_8 structure type) into FeAl (CsCl
 257 structure type) and $FeAl_2$ (triclinic, no other known structure of this type) occurs. The high
 258 temperature phase Fe_5Al_8 results from a peritectic reaction and, therefore, a two-phase field
 259 must be passed in order to obtain this phase during the solidification of this specific alloy. The
 260 according section of the equilibrium phase diagram is displayed in Figure 10a. The solid-state

261 decomposition results in a lamellar microstructure being potentially promising with respect to
262 its creep resistance in conjunction with the generally low density and very good oxidation
263 resistance of high Al containing iron aluminides.

264 Diffraction patterns obtained during directional solidification of this alloy within the FlexiDS
265 device are depicted in Figure 10b to e. The diffraction pattern in Figure 10b was obtained at the
266 solidification front, Figure 10 c,d and e in 3.5, 4.5 and 5.5 mm distance from the solidification
267 front respectively. The corresponding temperatures are indicated in Figure 10a. As seen in
268 Figure 10c, only Fe_5Al_8 appears within the single-phase region. Retardation of the phase
269 formation and excess FeAl_2 due to the slow peritectic reaction were not observed. The 2d
270 diffraction pattern in Figure 10 c, d and e were converted to 1d. The corresponding 1d
271 diffraction pattern are presented in Figure 11. Lattice parameters were found to be similar to
272 those reported by Stein et al. [33] for cast material. In contrast to expectations in Ref. [20] there
273 is no evidence for preferential orientation of the high temperature phase with respect to the
274 solidification direction even though a rather large range of withdrawal rates was tested, namely
275 6 to 240 mm/h. Nevertheless, columnar Fe_5Al_8 grains form at high withdrawal rates which
276 results in columnar eutectoid colonies after completion of the eutectoid reaction. For
277 withdrawal rates higher than 120 mm/h, inhomogeneous intensity distributions for the (001),
278 (010), and (011) diffraction rings of FeAl_2 indicative of a crystallographic texture are observed
279 in Figure 12a. Indeed, a majority of the lamellae in the eutectoid microstructure are aligned
280 with respect to the temperature gradient as seen in Figure 12b. For a single orientation of Fe_5Al_8 ,
281 twelve different orientation variants of the lamellae could be expected based on the distinct
282 orientation relationship of FeAl and FeAl_2 [20]. Obviously, high withdrawal rates lead to a
283 variant selection of the colonies in the temperature gradient during the eutectoid reaction even
284 though the parent phase does not exhibit preferential orientation. Without the application of in-
285 situ observation of the solidification and cooling process, this information would not have been
286 accessible.

287



288

Figure 10: (a) Section of the equilibrium Fe-Al phase diagram close to the eutectoid decomposition of Fe_5Al_8 into FeAl and FeAl_2 [32], (b) to (e) diffraction patterns obtained at four different temperatures as highlighted in (a).

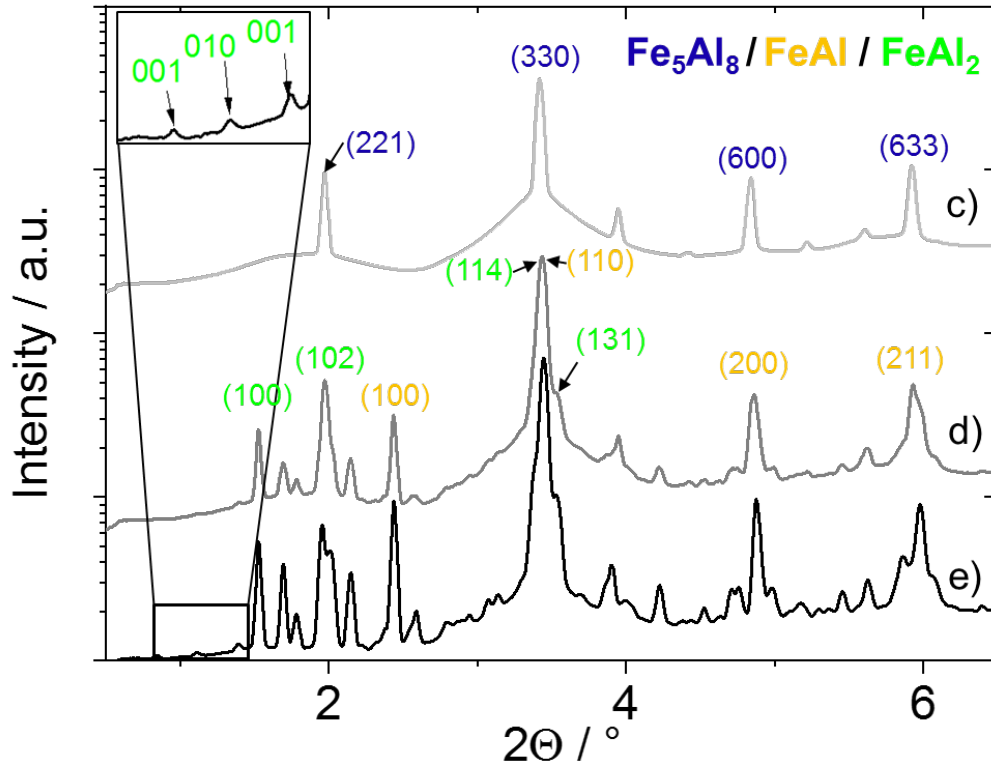


Figure 11: Converted 2d diffraction pattern to 1d diffraction pattern corresponding to Figure 10

c

to

e.

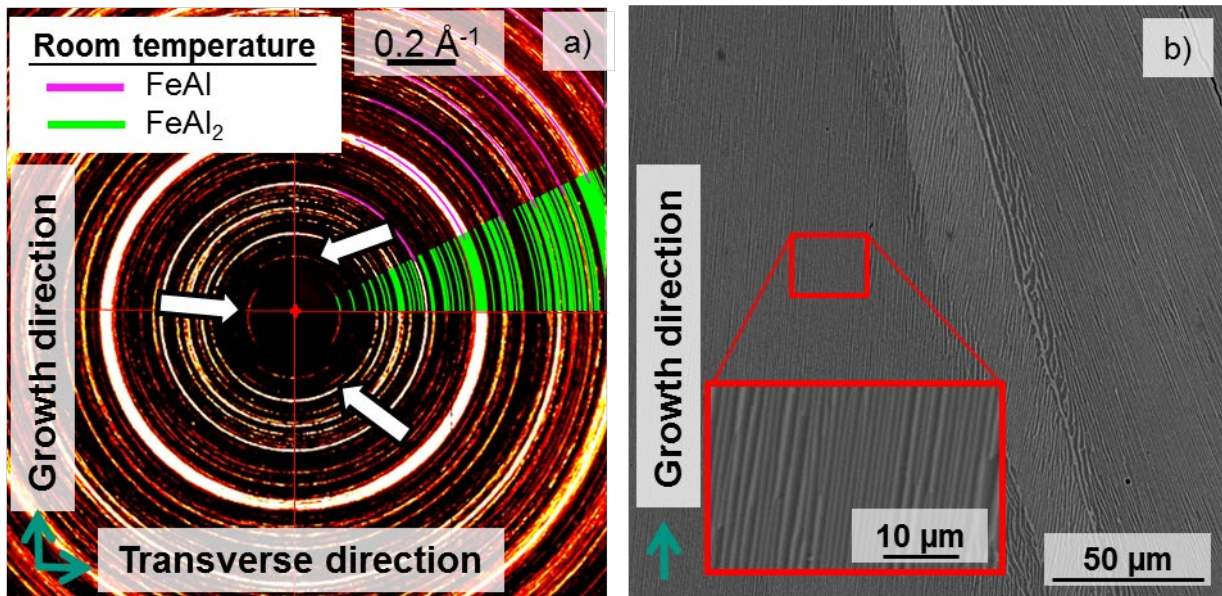


Figure 12: (a) Diffraction pattern of Fe-61Al at room temperature subsequent to directional solidification at 120 mm/h. Slight crystallographic texture is obtained for FeAl₂ indicated by inhomogeneous intensity distribution along the (001), (010), and (011) diffraction rings highlighted with arrows. (b) Scanning electron micrograph (backscatter electron imaging) of a longitudinal section of the directionally solidified material (bright phase is FeAl and dark phase is FeAl₂).

6. Summary

290 We introduced the new state-of-the-art FlexiDS device for time-resolved in-situ investigation
291 of directional solidification processes using high-energy synchrotron radiation. The system is a
292 valuable addition to the infrastructure of PETRA III at DESY, being specifically designed for
293 use at P07 HEMS beamline. The apparatus is capable of investigating liquid-solid regions,
294 transformations, and decompositions in various structural intermetallic materials. Moreover,
295 we could show the wide operation range by means of sample geometry, densities and alloy
296 compositions as well as process parameter like withdrawal rate. Even during experiments,
297 which exceed a liquidus temperature of 2000 °C, the device operated stable and satisfactory
298 diffraction pattern were obtained. Trial tests of time-resolved processes of TiAl and FeAl alloys
299 were presented in this work. Further detailed experimental results are forthcoming and will be
300 published elsewhere, for instance Ref. [22]. Not being installed at the beamline, the FlexiDS
301 device is available at the Helmholtz-Zentrum Geesthacht. There possible trial test of new alloys
302 can be performed without using high-energy synchrotron radiation in order to get used to the
303 device. We strongly welcome and encourage collaboration from the materials science research
304 community in order to maximize the potential of this unique in-situ directional solidification
305 device for improving understanding of fundamental solidification processes.
306

Acknowledgements

307 This research was financially supported by the German Federal Ministry of Education and
308 Research (BMBF) program “FlexiDS” (05K2016).
309 The authors acknowledge S. Huisl and M. Gleichmann from Systec Group and W. Ripp from
310 iTG for the manufacturing and implementation of the FlexiDS device and for the close
311 cooperation.
312 We are grateful to D. Matthiessen for the helpful experimental support.

References

- 313 [1] R.C. Reed, *The Superalloys: Fundamentals and Applications*, Cambridge University
314 Press, Cambridge (2006).
- 315 [2] T. Haenschke, A. Gali, M. Heilmaier, M. Krüger, H. Bei, E.P. George, Synthesis and
316 characterization of lamellar and fibre-reinforced NiAl-Mo and NiAl-Cr, *J. Phys. Conf.*
317 *Ser.* 240 (2010) 012063. doi:10.1088/1742-6596/240/1/012063.
- 318 [3] H. Bei, E.P. George, Microstructures and mechanical properties of a directionally
319 solidified NiAl–Mo eutectic alloy, *Acta Mater.* 53 (2005) 69–77.

- 320 doi:10.1016/j.actamat.2004.09.003.
- 321 [4] H.E. Cline, J.L. Walter, E. Lifshin, R.R. Russell, Structures, faults, and the rod-plate
322 transition in eutectics. *Metall. Trans. 2* (1971) 189–194. doi:10.1007/BF02662656.
- 323 [5] H.E. Cline, J.L. Walter, The effect of alloy additions on the rod-plate transition in the
324 eutectic NiAl-Cr. *Metall. Trans. 1* (1971) 2907–2917, doi:10.1007/BF03037830.
- 325 [6] G. Frommeyer, R. Rablbauer, H.J. Schaefer, Elastic properties of B2-ordered NiAl and
326 NiAl-X (Cr, Mo, W) alloys. *Intermetallics 18* (2010) 299–305.
327 doi:10.1016/j.intermet.2009.07.026
- 328 [7] A. Misra, R. Gibala, R.D. Noebe, Optimization of toughness and strength in multiphase
329 intermetallics. *Intermetallics 9* (2001) 971–978. doi:10.1016/S0966-9795(01)00098-X.
- 330 [8] C. Seemüller, M. Heilmaier, T. Haenschke, H. Bei, A. Dlouhy, E.P. George, Influence
331 of fiber alignment on creep in directionally solidified NiAl–10Mo in-situ composites.
332 *Intermetallics 35* (2010) 110–115. doi:10.1016/j.intermet.2012.12.007.
- 333 [9] D.R. Johnson, X.F. Chen, B.F. Oliver, R.D. Noebe, J.D. Whittenberger, Processing and
334 mechanical properties of in-situ composites from the NiAl-Cr and the NiAl-(Cr,Mo)
335 eutectic systems. *Intermetallics 2* (1995) 99–113. doi:10.1016/0966-9795(95)92674-O.
- 336 [10] J.D. Whittenberger, S.V. Raj, I.E. Locci, J.A. Salem, Effect of growth rate on elevated
337 temperature plastic flow and room temperature fracture toughness of directionally
338 solidified NiAl-31Cr-3Mo. *Intermetallics 7* (1999) 1159–1168. doi:10.1016/S0966-
339 9795(99)00023-0.
- 340 [11] N. Shevchenko, S. Boden, G. Gerbeth, S. Eckert, Chimney Formation in Solidifying
341 Ga-25 wt pct In Alloys Under the Influence of Thermosolutal Melt Convection, *Metall.*
342 *Mater. Trans. A.* 44 (2013) 3797–3808. doi:10.1007/s11661-013-1711-1.
- 343 [12] N. Shevchenko, O. Roshchupkina, O. Sokolova, S. Eckert, The effect of natural and
344 forced melt convection on dendritic solidification in Ga-In alloys, *J. Cryst. Growth.*
345 417 (2015) 1–8. doi:10.1016/j.jcrysgr.2014.11.043.
- 346 [13] A. Saad, C.-A. Gandin, M. Bellet, N. Shevchenko, S. Eckert, Simulation of Channel
347 Segregation During Directional Solidification of In-75 wt pct Ga. Qualitative
348 Comparison with In Situ Observations, *Metall. Mater. Trans. A.* 46 (2015) 4886–4897.
349 doi:10.1007/s11661-015-2963-8.
- 350 [14] SYSTEC Fertigungstechnik GmbH & Co.KG, Products (2020). Retrieved from
351 <https://www.systec-fertigungstechnik.de/produkte/maschinen-und-anlagenbau.html>
- 352 [15] iTG Induktionsanlagen GmbH (2020), Retrieved from <https://www.itg-induktion.de/en/home,02.06.2020>
- 353
- 354 [16] hema electronic, Products (2020). Retrieved from
355 <https://www.hema.de/en/services/products/seelector-icam-weld>
- 356 [17] Advanced Energy, Products (2020). Retrieved from
357 <https://www.advancedenergy.com/products/temperature-measurement/thermal-measurement-optical-pyrometers-power-controllers/metal-applications-pyrometers/impac-is-5-iga-5/>
- 358
- 359
- 360 [18] N. Schell, A. King, F. Beckmann, T. Fischer, M. Müller, A. Schreyer, The High
361 Energy Materials Science Beamline (HEMS) at PETRA III, *Mater. Sci. Forum.* 772
362 (2013) 57–61. doi:10.4028/www.scientific.net/MSF.772.57.

- 363 [19] N. Schell, The High Energy Materials Science Beamline of Helmholtz-Zentrum
 364 Geesthacht (HZG) and DESY (2020). Retrieved from [http://photon-](http://photon-science.desy.de/facilities/petra_iii/beamlines/p07_high_energy_materials_science/index_eng.html)
 365 [science.desy.de/facilities/petra_iii/beamlines/p07_high_energy_materials_science/inde](http://photon-science.desy.de/facilities/petra_iii/beamlines/p07_high_energy_materials_science/index_eng.html)
 366 [x_eng.html](http://photon-science.desy.de/facilities/petra_iii/beamlines/p07_high_energy_materials_science/index_eng.html)
- 367 [20] A. Scherf, A. Kauffmann, S. Kauffmann-Weiss, T. Scherer, X. Li, F. Stein, M.
 368 Heilmaier, Orientation relationship of eutectoid FeAl and FeAl₂, *J. Applied Crystal.* 49
 369 (2016) 442-449. doi.org/10.1107/S1600576716000911.
- 370 [21] F. Gang, A. Kauffmann, M. Heilmaier, *Metalurgical and Materials Transactions A* 49
 371 (2018) 763-771. doi.org/10.1007/s11661-017-4367-4.
- 372 [22] C. Gombola, A. Kauffmann, G. Geramifard, M. Blankenburg, M. Heilmaier,
 373 Microstructural investigations of novel high temperature alloys based on NiAl-
 374 (Cr,Mo), *Metals* 10 (2020) 961. doi.org/10.3390/met10070961.
- 375 [23] G. Hasemann, S. Ida, L. Zhu, T. Iizawa, K. Yoshimi, M. Krüger, Experimental
 376 assessment of the microstructure evolution and liquidus projection in the Mo-rich Mo-
 377 Si-B system, *Mater. Des.* 185 (2020) 108233. doi.org/10.1016/j.matdes.2019.108233.
- 378 [24] M. Oehring, V. Küstner, F. Appel, U. Lorenz, Analysis of the solidification
 379 microstructure of multi-component γ -TiAl alloys, *Materials Science Forum* 539-543
 380 (2007) 1475-1480. doi.org/10.4028/www.scientific.net/MSF.539-543.1475.
- 381 [25] B.P. Bewlay, S. Nag, A. Suzuki, M. J. Weimer, TiAl alloys in commercial aircraft
 382 engines, *Materials at High Temperatures* 33 (2016) 549-559.
 383 doi.org/10.1080/09603409.2016.1183068.
- 384 [26] M. Todai, T. Nakano, T. Liu, H.Y. Yasuda, K. Hagihara, K. Cho, M. Ueda, M.
 385 Takeyama, Effect of building direction on the microstructure and tensile properties of
 386 Ti-48Al-2Cr-2Nb alloy additively manufactured by electron beam melting, *Additive*
 387 *Manufacturing* 13 (2017) 61-70. doi.org/10.1016/j.addma.2016.11.001.
- 388 [27] M. Thomas, T. Malot, P. Aubry, C. Colin, T. Vilaro, P. Bertrand, The prospects for
 389 additive manufacturing of bulk TiAl alloy, *Materials at High Temperatures* 33 (2016)
 390 571-577. doi.org/10.1080/09603409.2016.1171510.
- 391 [28] S. Mayer, P. Erdely, F.D. Fischer, D. Holec, M. Kasthuber, T. Klein, H. Clemens,
 392 Intermetallic β -Solidifying γ -TiAl Based Alloys – From Fundamental Research to
 393 Application, *Adv. Eng. Mat.* 19 (2017), art. no. 1600735.
 394 doi.org/10.1002/adem.201600735
- 395 [29] M. Yamguchi, H. Inui and K. Ito, High-Temperature Structural Intermetallics, *Acta*
 396 *Mater.* 48 (2000) 307-322. doi.org/10.1016/S1359-6454(99)00301-8.
- 397 [30] O. Hunziker, M. Vandyoussefi, W. Kurz, *Acta Mater.* 46 (1998) 6325-6336.
 398 doi.org/10.1016/S1359-6454(98)00336-X.
- 399 [31] C. McCullough, J.J. Valencia, C.G. Levi, and R. Mehrabian, *Acta Metall.* 37 (1989)
 400 1321-1336. doi.org/10.1016/0001-6160(89)90162-4.
- 401 [32] X. Li, A. Scherf, M. Heilmaier, F. Stein, The Al-rich part of the Fe-Al phase diagram,
 402 *J. Phase Equilibria Diffus.* 37 (2016) 162-173. doi.org/10.1007/s11669-015-0446-7.
- 403 [33] F. Stein, S.C. Vogel, M. Eumann, M. Palm, Determination of the crystal structure of
 404 the ϵ phase in the Fe-Al system by high-temperature neutron diffraction, *Intermetallics*
 405 18 (2010) 150-156. doi.org/10.1016/j.intermet.2009.07.006.